

# Incorporating Streams into Milky Way Models

Nathan Deg<sup>1\*</sup>, Lawrence Widrow<sup>1</sup>

<sup>1</sup>*Department of Physics, Engineering Physics, and Astronomy, Queen's University, Kingston, ON, K7L 3N6, Canada*

29 March 2021

## ABSTRACT

We develop a framework for modelling the Milky Way using stellar streams and a wide range of photometric and kinematic observations. Through the use of mock data we demonstrate that a standard suite of Galactic observations leads to degeneracies in the inferred halo parameters. We then incorporate a GD-1-like stream into this suite using the orbit-fitting technique and show that the streams reduces the uncertainties in these parameters provided all observations are fit simultaneously. We also explore how the assumption of a disk-halo alignment can lead unphysical models. Our results may explain why some studies based on the Sagittarius stream find that the halo's intermediate axis is parallel to the disk spin axis even though such a configuration is highly unstable. Finally we show that both longer streams and multiple streams lead to improvements in our ability to infer the shape of our dark halo.

**Key words:** Galaxy: structure Galaxy: halo Galaxy: kinematics and dynamics

## 1 INTRODUCTION

In principle, a detailed model of the Milky Way's (MW) gravitational potential can be used to infer the shape and structure of the Galaxy's dark matter (DM) halo. The implications of such a determination range from dark matter detection to cosmological structure formation to galaxy evolution in the present-day Universe.

In any attempt to infer Galactic structure from data it is necessary to specify the space of Galactic models under consideration,  $M$ , the data,  $D$ , and the means by which one compares the two. The latter is often expressed in terms of a likelihood function,  $p(D|M)$ . In Bayesian statistics, one also specifies a prior probability on the model and then inverts the likelihood function to obtain the probability of the model given the data,  $p(M|D)$ .

Galaxy models are fraught with degeneracies, particularly when the set of observational constraints are limited. For example, models of external galaxies that are constrained by the rotation curve and surface brightness profile are plagued by the disk-halo degeneracy. These data are found in the plane of the disk making them insensitive to the halo shape and structure, thereby allowing one to trade off the disk and halo when fitting the predicted circular speed (see Courteau et al. (2013) and references therein). The disk-halo degeneracy leads to uncertainties in the local DM density and the stability of the disk against the formation of a bar or spiral structure.

In principle model degeneracies can be broken by combining different types of observations that sample different regions of the Galaxy. Stellar streams are a particularly promising and relatively new class of Galactic observations. These roughly one-dimensional stellar features are presumably formed when stars are stripped from dwarf galaxies by the tidal field of the host. They are located throughout the halo at a variety of radii which allows them to probe the shape and structure of the halo itself and break degeneracies like the disk-halo degeneracy. The Sagittarius (Sgr) stream is perhaps the most prominent example of a stellar stream and has been mapped over  $\sim 300^\circ$  across the sky. Soon after its discovery (Ibata et al. 1997) astronomers began modelling the MW using the stream in an effort to infer the Galactic potential. Some early examples include Ibata et al. (2001), Helmi (2004), Martínez-Delgado et al. (2004), Johnston, Law, & Majewski (2005), and Fellhauer et al. (2006).

Recently Law et al. (2009) utilized the Sgr stream to model the MW. Their Galactic model consists of a Hernquist bulge, a Miyamoto-Nagai disk, and a triaxial logarithmic. The halo was oriented so that one of its symmetry axes coincides with the spin axis of the disk and is characterized by five parameters: the scale length, the scale velocity, the axis ratios of the halo potential, and the orientation angle of the disk-plane symmetry axes. Of these parameters, Law et al. (2009) only explored the axis ratios and orientation. The halo scale length, as well as the bulge and disk parameters, are fixed to preferred values based on previous work (Law et al. 2010). The halo scale velocity was adjusted

\* E-mail: ndeg@astro.queensu.ca

so that the circular speed remains constant. The Sgr stream data used in their fit consisted of the M giant survey from Majewski et al. (2003) and Sloan Digital Sky Survey (SDSS) observations from Belokurov et al. (2006). The stream itself was modeled under the assumption that it traces the orbit of a single particle in a fixed potential (the orbit-fitting technique). Through a grid search of their three free parameters they found that a favored model with isopotential axis ratios of  $1.5 : 1.25 : 1$ .

Law & Majewski (2010) refined the work of Law et al. (2009) by using N-body methods to model formation of the stream. They found that the dark halo had *isopotential* axis ratios of  $1.28 : 1.26 : 1$  with the intermediate axis perpendicular to the Galactic disk and the short axis roughly along the Sun-Galactic Center line. Deg & Widrow (2013), using a different Galactic model, performed a Bayesian analysis of the Sgr stream and a suite of other observational constraints and found the halo to have isodensity axis ratios of  $3.3 \pm 0.7 : 2.7 \pm 0.4 : 1$  with almost the same orientation. However, Ibata et al. (2013) used the streak-line method (Varghese et al. 2011; Küpper et al. 2012) for the stream model and found that they could fit the stream observations using a Galactic model with a spherical, non-parametric halo. Additionally, Vera-Ciro & Helmi (2013) used a similar model to Law et al. (2009) but allowed the halo shape to change with radius. They found results similar to Law & Majewski (2010), but, when they included the effect of the Large Magellanic Cloud on the stream, the inferred halo shape was only mildly triaxial.

The Sgr stream is particularly difficult to model. It is dynamically hot and has a complicated structure. Belokurov et al. (2014) recently showed that the trailing arm has a different apocenter than the leading arm. Peñarrubia et al. (2010) has shown that the stream structure depends on the progenitor's structure as well as the MW. Moreover, Zhao (2004) has shown that the orbit of Sgr is unlikely unless it is particularly massive or fell in with a group. As such, its orbital properties are likely quite complex and difficult to model. Finally, the stream shows an apparent bifurcation in both the leading and trailing arms Fellhauer et al. (2006). It is unclear whether this bifurcation is due to the formation of the stream, from some secondary companion, or whether it is a completely different stream altogether (Koposov et al. 2012). No study has yet been able to fit all these observations.

A number of studies have used other observed streams to model the MW. Willet et al. (2009) found an orbit fit for the GD-1 stream (discovered by Grillmair & Dionatos (2006)) but were unable to derive a constraint on the halo shape. However, Koposov et al. (2010) obtained 6-D phase space information on the stream. Using the orbit fitting technique with this data, they found the total potential to be oblate with the short axis perpendicular to the disk. They note that this flattening may be mostly due to the disk. When they include the disk mass uncertainties they were unable to find robust constraints on the halo flattening. Newberg et al. (2010) modeled the Orphan stream (independently discovered by Grillmair (2006) and Belokurov et al. (2007)) using the orbit-fitting technique, but found that a longer stream is needed to distinguish between a variety of different MW models as many of their model orbits diverged significantly past the edge of the data.

Lux et al. (2012) fit orbits for the NGC 5466 stream (discovered by Belokurov et al. (2006b); Grillmair & Johnson (2006)) in a variety of Galactic models. They found that only orbits in oblate or triaxial potentials produce deviations in the angular position that mark turning points in the orbit. There are hints that such kinks are present in the stream data, suggesting a non-spherical halo. Grillmair & Dionatos (2006b) attempted to find orbits for the Palomar 5 (Pal 5) stream (discovered by Odenkirchen et al. (2001)) and found that a spherical halo fit the data reasonably well. From this sample of studies, it is clear that MW models generated using stellar streams vary greatly. These variations are due to differences in three key elements of the analysis: the space of models examined, the data used as constraints, and the method for modeling the stream.

Today there are roughly a dozen known Galactic streams (see Sanders & Binney (2013) for a summary). The launch of Gaia (Perryman et al. 2001) will surely lead to the discovery of new streams and improvements in the observational constraints from known streams. With Gaia in mind, we set out to carefully examine how streams can be combined with other Galactic observations to break some of the existing degeneracies in the halo structure and shape parameters. We utilize mock data for this examination and model streams using the orbit-fitting technique. This allows us to sidestep the issue of how best to model streams and focus on issues relating to the space of Galactic models, the data used to constrain those models, and the construction the likelihood function.

This study is complementary to the recent work of Lux et al. (2013). They explore the biases that arise in the inferred halo shape due to the use of the orbit-fitting technique on realistic streams using mock data. Both our work and Lux et al. (2013) use Markov Chain Monte Carlo (MCMC) techniques to explore a parameter space, but we utilize non-stream constraints and explore a substantially larger parameter space.

We begin in Section 2 by describing a three-component MW model. In Section 3 we present a suite of Galactic observations that constrain the model. We also describe our procedure for generating mock data for a MW-like galaxy. In Section 4 we examine some of the degeneracies that are found in the model parameters when we fit only the suite of standard constraints, as well as where those constraints arise. In Section 5 we present the stream observations, stream fitting algorithm, and mock data. In Section 6 we show that streams observations must be combined all other constraints simultaneously to get the best constraints possible for the halo shape. We then demonstrate how the potentially erroneous assumption of a disk-halo alignment, can affect the inferred parameters. We finish Section 6 by examining the halo shape and orientation when a GD-1-like stream is combined with the full suite of constraints and the full model parameter space is explored. In Section 7 we show how the use of either a longer stream or multiple streams provide leads to improvements in our ability to infer the shape of the dark halo.

## 2 GALACTIC MODEL

We model the Galactic density as a Sérsic bulge, an exponential disk, and a triaxial Einasto halo Einasto (1965). An alternative and popular approach is to model the Galactic potential in terms of analytic functions (some examples include Law & Majewski (2010), Vera-Ciro & Helmi (2013) and Newberg et al. (2010)). It is computationally simpler to calculate forces from an analytic potential than it is to obtain the force by integrating the density. However, cosmological simulations suggest that it is the halo density rather than the potential that is triaxial (Frenk 1988; Franx, Illingworth, & de Zeeuw 1991; Warren et al. 1992; Jing & Suto 2002; Allgood et al. 2006). Indeed a triaxial potential can lead to peanut shaped densities, and, in extreme cases, negative values for the density (Binney & Tremaine 2008). For this reason we model the Galaxy using density functions.

The bulge density that generates a Sérsic profile in projection is (Prugniel & Simien 1997; Terzić & Graham 2005)

$$\rho_b(r) = \frac{\sigma_b^2 C(n)}{4\pi G R_e^2} \left(\frac{r}{R_e}\right)^{-p} e^{-b(r/R_e)^{1/n}}, \quad (2.1)$$

where  $n$  is the Sérsic index,  $p = 1 - 0.6097/n + 0.05563/n^2$ ,  $C(n) = nb^{n(p-2)}\Gamma(n(2-p))$ , and  $b = b(n)$  is chosen so that the radius  $R_e$  encloses half the total projected mass. An analytic expression for the associated potential can be found in Terzić & Graham (2005)

The disk density is

$$\rho_d(R, z) = \frac{M_d}{4\pi R_d^2 z_d} e^{-R/R_d} \text{sech}^2(z/z_d) \quad (2.2)$$

where  $M_d$ ,  $R_d$ , and  $z_d$ , are the disk mass, radial scale length, and vertical scale height. The Einasto halo density (Einasto 1965; Merritt et al. 2005) is

$$\rho_h(r_t) = \rho_0 e^{-\frac{2}{\alpha}((r_t/r_h)^\alpha - 1)}, \quad (2.3)$$

where,  $\rho_0$ ,  $r_h$ , and  $\alpha$  are the halo scale density, scale radius, and a parameter to control the logarithmic slope respectively. The triaxial radius,  $r_t$ , in component notation, is

$$t_{t,i} = R_{i,j} \Lambda_{j,k} r_k, \quad (2.4)$$

where  $\Lambda$  is a diagonal matrix with elements  $(1, A, B)$  where  $A \geq 1 \geq B$  and  $\mathbf{R}$  is an Euler rotational matrix made of consecutive rotations about the  $Z$ ,  $Y$ , and  $X$  axes. This set up means that  $A$  is the major/intermediate axis ratio,  $B$  is the minor/intermediate axis ratio, and the first two Euler angles give the angular position of the intermediate axis. In our analysis we simply use logarithmic priors for  $A$  and  $B$ .

The potential for the halo is found using the homeoid theorem (see Binney & Tremaine (2008)). When the coordinate axes are aligned with the symmetry axes, the halo potential is

$$\Phi(\mathbf{x}) = -\pi G \frac{a_2 a_3}{a_1} \int_0^\infty d\tau \frac{\psi(\infty) - \psi(m)}{\sqrt{(\tau + a_1^2)(\tau + a_2^2)(\tau + a_3^2)}} \quad (2.5)$$

where  $a_i$  are the axis ratios,

$$m^2 = a_1^2 \sum_{i=1}^3 \frac{x_i^2}{a_i^2 + \tau} \quad (2.6)$$

is similar to the square of the ellipsoidal radius, and

$$\psi(m) = \int_0^m dm^2 \rho(m^2) \quad (2.7)$$

is an auxiliary function. From the definition of the halo shape  $a_1 = 1$ ,  $a_2 = A$ , and  $a_3 = B$ .

The disk potential is found using the technique of Kuijken & Dubinski (1995). An analytic 'fake' disk density-potential pair,  $(\rho_{fd}, \Phi_{fd})$  is constructed so that  $\rho_d = \rho_{fd} + \rho_r$  and  $\Phi_d = \Phi_{fd} + \Phi_r$  where  $(\rho_r, \Phi_r)$  is the density-potential pair of the residual. The fake disk is designed to account for the high-order moments that arise due to the thinness of the disk. The Poisson equation is solved via spherical harmonics up to  $l = 2$  for  $\Phi_r$  in an iterative scheme and summed with the analytic fake disk potential.

## 3 THE LIKELIHOOD FUNCTION, OBSERVATIONAL CONSTRAINTS, AND MOCK DATA

In this section we present the likelihood function that is used to evaluate a particular model. We then discuss the various non-stream observations used for constraining the Galactic model as well as the generation of mock data.

### 3.1 The Likelihood Function

Bayesian statistics provides a method for calculating the probability of a particular model given some data. From Bayes theorem, the model's probability, called the posterior is

$$p(M|D, I) = \frac{p(M|I)p(D|M)}{p(D|I)}, \quad (3.1)$$

where  $I$  represents prior information,  $p(M|I)$  is the prior probability on the model  $M$ , and  $p(D|M)$  is the likelihood of the data given the model. The term  $p(D|I)$ , often referred to as the evidence, is essentially a normalization factor and does not enter our calculations.

The prior probability is simply the product of the prior probabilities for each free parameter. Similarly, the likelihood is the product of the likelihood for each individual data point, regardless of the type of data, i.e. angular position, radial velocity, etc. We assume that all errors are Gaussian so that the likelihood of any given data point is simply

$$p(D_{i,j}|M) = \frac{1}{\sqrt{2\pi\sigma_{i,j}^2}} e^{\frac{M_{i,j} - D_{i,j}}{2\sigma_{i,j}^2}}, \quad (3.2)$$

where the  $D_{i,j}$  is the  $i$ 'th data point of the  $j$ 'th type of observational constraint,  $\sigma_{i,j}$  is the corresponding error, and  $M_{i,j}$  is the model prediction.

In order to fully map out the posterior distribution function (PDF) of the large parameter space we utilize the EMCEE algorithm from Foreman-Mackey et al. (2012). This Markov Chain Monte Carlo (MCMC) scheme is based on the Stretch-Move affine invariant algorithm found in Goodman & Weare (2010) and scales particularly well with the number of parameters. The chain is comprised of an ensemble of 'walkers' that explore the parameter space. The proposal for a given walker is generated in two steps. First,

a second walker is randomly chosen. Then a line in parameter space is drawn connecting the current state of the two walkers. Finally a random number is selected from a square-root distribution to determine the length along the line one 'stretches' to select the proposal.

We modify the EMCEE algorithm in two ways. Firstly we account for the fact that the Euler angles are essentially the product of a sphere with a circle. We describe the modification needed to deal with this non-trivial topology in the Appendix. Secondly, we include simulated annealing for stream constraints (Gregory 2005). We found that the stream constraints often contained a number of false minima and the chain became stuck. Simulated annealing slowly cools the stream likelihood, which allows the chain to avoid being trapped by these false minima. If we define the likelihood of some type of observation as  $\mathcal{L}_j = \sum_i \ln(p(D_{i,j}|M))$  then, with annealing, the likelihood is

$$\mathcal{L} = \sum_j^{\text{suite}} \mathcal{L}_j + \beta(t) \sum_j^{\text{streams}} \mathcal{L}_j, \quad (3.3)$$

where  $\beta(t)$  is the annealing temperature. The total likelihood is  $p(D|M) = e^{\mathcal{L}}$ . We slowly increase  $\beta$  from  $10^{-4}$  to 1 in logarithmic intervals over 1000 MCMC steps. The simulated annealing closely resembles the parallel tempering found in Varghese et al. (2011).

### 3.2 Observational Constraints

In this work we use the suite of non-stream constraints found in Deg & Widrow (2013), which followed the work of Widrow et al. (2008) and Dehnen & Binney (1998), and comprises observations of the Oort constants, the local circular speed, the local surface density and vertical force, the inner and outer rotation curves, the bulge surface brightness and line-of-sight velocity dispersion, and the total mass within 100 kpc.

Briefly, Reid et al. (2009) used Very Long Baseline radio observations to determine trigonometric parallaxes and proper motions for masers throughout the Milky Way's disk. Bovy et al. (2009) reanalyzed these in conjunction with the proper motion of Sgr A\* to find a circular speed of  $v_c(R_o) = 244 \pm 13 \text{ km s}^{-1}$ . For the Oort constants, we use  $A = 14.8 \pm 0.8 \text{ km s}^{-1} \text{ kpc}^{-1}$  and  $B = -12.4 \pm 0.6 \text{ km s}^{-1} \text{ kpc}^{-1}$  from Feast & Whitelock (1997). We use the disk surface density measurement of  $\Sigma_d = 49 \pm 9 \text{ M}_\odot \text{ pc}^{-3}$  from Flynn & Fuchs (1994) and the vertical force measurement of  $|K_z(1.1 \text{ kpc})| = (2\pi G) 71 \pm 6 \text{ M}_\odot \text{ pc}^{-2}$ , from Kuijken & Gilmore (1991), which are in good agreement with similar studies (see, for example, Holmberg & Flynn (2004)). We will point out that the observations of the surface density are made with a 'rotation curve' prior that is equivalent to assuming a spherical halo. However, this study uses mock data self-consistently generated from a non-spherical model so any issues related to this prior are avoided.

For the bulge LOSVD we use the compilation of observations found in Tremaine et al. (2002) with the restriction that  $r \geq 4 \text{ pc}$  to avoid complications from the central black hole. Additionally, we adjust the dispersion upwards by a factor of 1.07 to account for the non-sphericity of the bulge.

For the surface brightness profile we use the infrared COBE-DIRBE observations (Binney, Gerhard, & Spergel 1997).

As is typical, we break the rotation curve constraints into an inner and outer portion. For the inner rotation we fit the peak velocities along particular lines-of sight. If the potential is axisymmetric the peak velocity is related to the circular speed by  $v_{\text{term}} = v_c(R) - v_c(R_o) \sin l$ . This approximation still holds for a triaxial model as the axisymmetric disk and bulge components dominate the potential of the inner disk. The data used is from Malhotra (1995) with the restriction that  $\sin l \geq 0.3$  so as to avoid distortions due to the bar.

The outer rotation curve is slightly more complicated. The line-of-sight velocity,  $v_{lsr}$ , is related to the circular speed in the expression

$$W(R) = \frac{R_o}{R} v_c(R) - v_c(R_o) = \frac{v_{lsr}}{\cos b \cos l}. \quad (3.4)$$

The data used consists of  $v_{lsr}$  observations of HII regions and reflection nebulae from Brand & Blitz (1993) and Carbon stars from Demers & Battinelli (2007). In order to avoid complications due to non-circular motions the data is restricted to  $l \leq 155^\circ$  or  $l \geq 205^\circ$ ,  $d \geq 1 \text{ kpc}$ , and  $W \leq 0$ . Additional 'noise' parameters are added to  $d$  and  $v_{lsr}$  to account for any unknown systematics. Therefore the error for the  $j$ 'th data point is  $\Sigma_{u,d}^2 = \sigma_{u,d}^2 + \epsilon_{u,d}^2$  where  $\sigma$  is the observed error,  $\epsilon$  is the noise parameter, and the  $u$  or  $d$  subscripts are for the distance and velocity respectively. Since the systematics may be different between the two data sets we use two sets of noise parameters. These calculated errors are then propagated through to errors in  $W$ .

### 3.3 Mock Data

The mock data is generated from a model that is designed to resemble the MW. To get a generative MW-like model we start by selecting a reasonable halo shape. Figure 1 of Allgood et al. (2006) shows that halos with masses  $\simeq 10^{12} \text{ M}_\odot$  typically have a minor to major axis ratio of  $\approx 0.60 \pm 0.02$ . Therefore we set the generative model's axis ratios to  $A = 1.25$  and  $B = 0.75$ . We also set the orientation so that the disk and halo are misaligned. The generative Euler angles are  $(45^\circ, 30^\circ, 10^\circ)$  which sets the halo's intermediate axis to be  $45^\circ$  from the Sun-Galactic Center line with a  $30^\circ$  inclination.

The rest of the parameters for the generative model are found by analyzing the suite of non-stream observations. The halo shape is fixed to that of the generative model and we run the EMCEE algorithm to sample the remaining parameter space. The model with the largest posterior is then selected to be the generative model. After rounding the results, the generative model's parameters are set to  $n = 1$ ,  $\sigma_b = 225 \text{ km s}^{-1}$ ,  $R_e = 0.8 \text{ kpc}$ ,  $M_d = 3.7 \times 10^{10} \text{ M}_\odot$ ,  $R_d = 2.7 \text{ kpc}$ ,  $z_d = 0.25 \text{ kpc}$ ,  $M/L_b = 0.55$ ,  $M/L_d = 0.8$ ,  $\rho_0 = 2.325 \times 10^{-3} \text{ M}_\odot \text{ pc}^{-3}$ ,  $r_h = 15 \text{ kpc}$ , and  $\alpha = 0.2$ . In addition to Galactic model's parameters, we also fit the Sun's location and peculiar velocity and find the peak at  $R_0 = 8 \text{ kpc}$ ,  $(u_\odot, v_\odot, w_\odot) = (-10 \text{ km s}^{-1}, -5.45 \text{ km s}^{-1}, 7.0 \text{ km s}^{-1})$ .

The procedure for generating mock data is similar to the procedure for calculating the likelihood. Just like the likelihood, we begin by calculating the model predictions

for each observation. Then we add an error term from the Gaussian corresponding to the observed error. This gives a mock data set with the same dispersion as the actual data.

#### 4 STANDARD SUITE EXPLORATION

In this section we explore degeneracies in the halo model that arise in the absence of stream constraints. We begin by analyzing the mock data with the halo shape fixed to that of the generative model. The left panel of Figure 1 shows the resulting PDF for the halo scale length and density. There is a clear degeneracy in these two parameters with the shape of the PDF being primarily determined by the local vertical force constraint. As shown in the middle and right panels of Figure 1, the vertical force remains approximately constant as one follows the  $\rho_{0,h} - r_h$  ridge seen in the left panel.

A second, complementary analysis is to fix the various Galactic parameters while allowing the shape parameter ( $A, B, \theta, \phi, \psi$ ) to vary. This approach is very similar to the approach used in many stream studies like Law & Majewski (2010), Vera-Ciro & Helmi (2013), and Koposov et al. (2010). The PDF for the axis ratios of this analysis are shown in the lower left panel of Figure 2. This panel shows that both  $A$  and  $B$  are poorly constrained by the model, with the  $1\sigma$  confidence interval on  $A$  ranging from 1 to  $\simeq 2.5$  and  $B$  ranging from  $\simeq 0.4$  to 1. Since the axis ratios are logarithmic, these two ranges are roughly equal. While some of the inferred models are clearly unphysical, they still fit the suite of observational constraints that are considered. The upper left and lower right panels show that once again, the local vertical force remains constant with either parameter.

#### 5 STREAM MODELLING AND DATA

In this section we discuss the orbit-fitting technique for modelling stellar streams and the production of mock streams of an arbitrary angular size. The mock data are motivated by observations of the GD-1 and Orphan streams.

##### 5.1 The Orbit-Fitting Technique

The orbit-fitting technique is based on the approximation that stellar streams trace the orbit of a particle in a fixed potential. In reality, the kinematics and morphology of the stream depends on the evolving tidal field of the host galaxy and the orbit and internal structure of the progenitor. The stream stars are stripped from the progenitor at the inner and outer Lagrange points leading to an offset between the orbit and the stream as well as a difference between the progenitor's orbital energy and the stream star's energy. Therefore using the orbit-fitting technique will introduce biases in the inferred quantities for real streams (Lux et al. 2013; Sanders & Binney 2013). N-body simulations are required to truly capture the full richness of the stream physics. However, for an MCMC-based parameter estimation scheme, such simulations are prohibitively expensive in terms of CPU time. There are a variety of other methods for modelling streams, including, but not limited to, the streak-line method (Varghese et al. 2011; Küpper et al. 2012) and the

action-angle technique (Sanders & Binney 2013), but they introduce additional model parameters and computational challenges. In this study we generate mock data that lies along the orbit and avoid the issue of biases due to the use of the orbit-fitting technique.

When using the orbit-fitting technique, one calculates the orbit of a 'progenitor' particle in the fixed potential. If the stream's actual progenitor is known the particle is placed at it's location. Otherwise, it is placed in the middle of the observed stream. The 'progenitor' particle has six-phase space coordinates that should be included as free model parameters. In practice, streams often have a thin enough angular thickness that one can fix the progenitor's position on the sky with no loss of generality.

Comparing the orbit to the stream data is fairly straightforward. First the orbital point that has the shortest angular distance on the sky to a given data point is found. This is not a trivial step as it requires a search of all calculated orbital points and an interpolation between those points that are closest to the data point. Once the appropriate orbital point is found, either its angular position, radial velocity, distance, or proper motions are compared to the data point using Eq. 3.2.

We also model the 'thickness' of the stream in each phase-space coordinate by replacing the observed errors with free parameters. These 'thickness' parameters represent the convolution of the observed error with the angular stream thickness, the internal velocity dispersion, and the spread in distances to the Sun.

##### 5.2 Stream Mock Data

As discussed in the introduction there are about a dozen currently known streams. The most well-known is the Sgr stream. Its thickness and internal structure make the use of the orbit-fitting technique for the stream model problematic. Instead we use the the GD-1 and Orphan streams. These streams are both long and thin, covering  $\sim 70^\circ$  and  $\sim 60^\circ$  of the sky respectively.

Koposov et al. (2010) provides observations of the full 6-D phase space for the GD-1 stream. We will use those observations as a basis for mock GD-1-like streams. Similarly, we will use the observations of the Orphan's stream angular position, radial velocity, and distance from Newberg et al. (2010) to generate mock Orphan-like streams.

The mock streams themselves are made from the orbit of a progenitor particle in the generative potential. The orbit is calculated and the mock data are found by adding the appropriate Gaussian error from the real data. For the angular position, the error is found perpendicularly to the orbit. Unlike the other mock data, which is observed at the same location as the real data, the mock stream data is spaced evenly along the orbit for an arbitrary angular size. However, the number of data points and type of observations are identical to the real data. The only difference is the length of the stream and the even spacing of the data.

#### 6 HALO SHAPE FROM A STELLAR STREAM

We begin by considering the case where the Galactic parameters are known and the stream data alone is used to

constrain the halo shape parameters. All other parameters are fixed to the generative value, except for the halo scale density, which is adjusted to keep the local circular speed equal to the generative model's value of  $207 \text{ km s}^{-1}$ . This case, while unrealistic, closely follows the procedure used in Law & Majewski (2010).

The inferred shape and orientation PDFs for this analysis are shown in the first three panels of the left-hand column of Figure 3. Both the inferred shape and orientation of the halo are highly degenerate. These poor constraints are due to the freedom of halo orientation. Since the progenitor location is fixed, the fit to the mock stream can be approximated as a fit to the force at the progenitor. The PDF of this force compared to the latitude of the intermediate axis is shown in the bottom left-hand panel of Figure 3. This panel shows that the force at GD-1 is almost as tightly constrained as the measurement of the local vertical force. Therefore, as long as the projection of the halo axes at some orientation provides roughly the same force at the progenitor location, the model will provide an acceptable fit to the stream data.

The second column of Figure 3 shows the results where the constraints from the stream are combined with the non-stream constraints (excluding the circular speed). The improvement in the inferred shape constraints is remarkable. While the constraints on the force at GD-1 have decreased by only  $\approx 20\%$  compared to the stream alone, the constraints on  $A$  and  $B$  have decreased to  $\sim 1 - 1.8$  and  $\sim 0.55 - 1$ , which are roughly equivalent in terms of the logarithmic priors. Evidently, the additional Galactic observations rule out many of the other models that fit the GD-1 stream.

It is worth comparing these results for mock data to the results of Koposov et al. (2010) for the actual GD-1 stream. They were able to find a constraint on the total flattening of the potential, but, when the uncertainty in the disk mass was considered, the constraints on the halo shape were quite poor. The right-hand panel of Figure 3 seems to contradict this conclusion. However, we are still fixing all the disk parameters and we are using many other observational constraints that were not considered in Koposov et al. (2010). It is more appropriate to compare the left-hand column of Figure 3 to their results. While a direct comparison is difficult, both our results and their Figure 18 show very poor constraints on the halo shape. It seems that the uncertainty introduced by the halo orientation affects the inferred shape in a similar manner as the uncertainty in the disk mass. However, it must be remembered that they are analyzing a stream while we are analyzing mock data generated from an orbit, which may also account for some of the differences in the quality of the inferences.

The PDFs for the GD-1-like stream plus the Galactic constraints represent a best-case scenario for stream modelling. The stream is traced by the orbit of a single particle and the majority of the Galactic parameters are known. Yet both  $A$  and  $B$  are still uncertain at the  $\pm 50\%$  level. The stream has significantly improved the constraints on the halo shape, but, when the halo orientation is allowed to vary, the uncertainties in the shape parameters are still quite large.

In reality the precise values of the various MW model parameters are not known and it is certainly possible that the use of incorrect values for the fixed model parameters may introduce systematic errors in the parameters of in-

terest. To illustrate this point, let us consider a common assumption in studies of stellar streams: that the disk and halo are aligned. To that end, we re-analyze our mock data, which were constructed from a model where the minor axis of the halo is the closest to the disk's spin axis but differs from the spin axis by  $30^\circ$ , under this assumption. In this re-analysis we allow all the parameters to vary except two of the Euler angles, forcing one of the halo symmetry axes to be parallel to the disk spin axis. We fit all the observational constraints, including the circular speed and the GD-1-like stream. For simplicity, we replace  $A$  and  $B$  with  $A'$  and  $B'$  where  $A'$  is the ratio of the larger axis in the plane of the disk to the smaller axis in the plane of the disk and  $B'$  is the ratio of the axis parallel to the disk spin axis to the smallest axis in the plane of the disk. The value of the smallest axis in the plane of the disk is set to one. Therefore,  $A'$  can refer to either the major or intermediate axis and  $B'$  can be the major, minor, or intermediate axis.

The PDF for  $A'$  and  $B'$  is shown in Figure 4. Any model with  $B' < 1$  has the minor axis parallel to the disk spin axis while any model with  $B' > 1$  has the major axis parallel to the disk spin axis. Figure 4 shows that our analysis overwhelmingly prefers models with the intermediate axis parallel to the disk spin axis. This disagrees with the generative model, which has the minor axis closest to the disk spin axis.

The result from this analysis may resolve a discrepancy in the literature about the Sgr stream. Both Law & Majewski (2010) and Deg & Widrow (2013) considered triaxial halos and assumed that the disk and halo were aligned. Using the Sgr stream, both studies found the intermediate axis of the halo was parallel to the disk spin axis. However, simulations by Debattista et al. (2013) show that such an alignment is unstable. Our results suggest that the alignment found by Law & Majewski (2010) and Deg & Widrow (2013) may be due to the assumption of that the disk and halo are aligned. We also note that this discrepancy may be caused by other assumptions in Law & Majewski (2010) and Deg & Widrow (2013). For instance, Vera-Ciro & Helmi (2013) showed fit the Sgr stream using a halo where the triaxiality varies with radius. Alternatively, Ibata et al. (2013) used a non-parametric spherical halo to fit the Sgr stream. Neither of these studies have results that disagree with Debattista et al. (2013). Furthermore, no study of the Sgr stream has been able to fit all the known Sgr data, including the bifurcation.

In order to avoid confusion and systematics that may arise due to incorrect assumptions about the model parameters, one should allow all the model parameters to vary according to their priors while fitting all possible observational constraints simultaneously. Figure 5 shows the results for an analysis where we follow such a procedure. These PDFs are marginally smaller than the for the suite of constraints alone and significantly smaller than for the GD-1 stream alone. In both of those cases the Galactic parameters were fixed, while in this case the parameters are completely free. When one considers the increased freedom, the improvement, whether marginal or significant, over an analysis with the Galactic parameters fixed reinforces the point of Figure 3. Constraints from stellar streams should be incorporated into a larger suite of Galactic constraints when modelling the MW.

As expected, the PDFs for the shape and orientation have increased in size relative to the second column of Figure 3. The  $1\sigma$  limits on  $A$  and  $B$  are now  $\sim 1-2$  and  $\sim 0.4-1$  compared to Figure 3's limits  $\sim 1-1.8$  and  $\sim 0.55-1$ . The area of the  $1\sigma$  shape contours in second column of Figure 3 is  $\approx 60\%$  of those in Figure 5. Nonetheless the contours of Figure 5 represent what can realistically be achieved in a best case scenario with a GD-1-like stream using the orbit-fitting method.

## 7 LONG STREAMS AND MULTIPLE STREAMS

Further observations may provide avenues to break the degeneracies in the shape parameters found in Figure 5. Firstly, one could use a single longer stellar stream in the model constraints. The longer stream should improve the constraints by reducing the number of possible orbits that fit the data as many of the orbits that fit a shorter stream diverge rapidly past the edge of the data.

To explore how much can be gained with an extended stream we generated a  $180^\circ$  GD-1-like stream. Combining that stream with the suite of other constraints we repeat the analysis of Section 5. The resulting shape PDFs are shown in Figure 6. In this case the  $1\sigma$  limits on  $A$  and  $B$  have been reduced to  $\simeq 1-1.5$  and  $\simeq 0.65-1$  respectively. This gives an area for the shape contours that is  $\approx 35\%$  of the area seen in Figure 5. The shape contours for the  $180^\circ$  stream where the full parameter space is explored are roughly equal to the inference with a  $70^\circ$  where only the shape and orientation parameters are explored.

A second idea to remove some of the degeneracies present in the model parameters is simply to utilize multiple stellar streams simultaneously. As a proof-of-concept, let us consider the  $70^\circ$  GD-1-like stream used previously and a  $60^\circ$  Orphan-like stream. Before combining the constraints from the two streams, we analyzed the Orphan-like stream together with the Galactic constraints. As with the GD-1 stream, we fix the angular position of the progenitor particle to the middle of the mock stream while varying the other four phase-space coordinates. The shape and orientation PDFs for that analysis are shown in Figure 7. In this case the constraints on the shape and orientation are worse than those for GD-1. However, it should be noted that the mock data for the Orphan-like stream contains significantly fewer data points than the GD-1-like stream and does not include proper motions.

The PDFs for the combination of the two streams are shown in Figure 8. The shape contours have improved from those of Figure 4, while the orientation contours appear to be slightly worse. Here the absolute  $1\sigma$  limits on  $A$  and  $B$  are  $\simeq 1-1.6$  and  $\simeq 0.5-1$  respectively. Additionally, the PDF contains a ridge that reduces the area of the  $1\sigma$  contours. Ultimately, area contained in axis ratio contours for two streams is equivalent to the area for a single  $180^\circ$  long GD-1-like stream.

## 8 CONCLUSIONS

In this work we have examined how stellar streams can be used to remove some of the degeneracies found in MW models. In our view one of the main takeaway points of this study is that in modelling the MW, one should apply Galactic and stream constraints simultaneously while exploring the full parameter space. Figure 3 clearly shows that the full suite of Galactic observations, which include local measurements of the vertical force, circular speed, and Oort constants provide useful information on the halo shape. A comparison of Figure 5 and Figure 3 shows that the standard practice whereby one fixes the structural parameters of the disk, bulge, and spherically-averaged halo while fitting the axis ratios and orientation of the halo may lead one to over-estimate the extent to which stream observations constrain the shape of the dark halo.

A second lesson is one should avoid restrictive model assumptions such as an alignment between the symmetry axis of the disk and one of the symmetry axes of the halo. Indeed, it appears that it is precisely this assumption that lead Law & Majewski (2010) and Deg & Widrow (2013) to the unphysically unstable model wherein the disk sits in the plane defined by the major and minor axis (Debattista et al. 2013). When we relax the assumption of disk-halo alignment and fully explore the parameter space we are able to recover the shape and orientation of the halo with uncertainties on the order of  $\simeq 50\%$ . In this respect, our paper complements that of Ibata et al. (2013), where the lesson is that models that assume a particular form for the spherically-averaged halo density profile may be too restrictive.

The third point of this paper is that the use of extended streams or multiple streams improve the constraints on the halo shape significantly. However, our analysis of mock data suggests that, at best, combining observation of the GD-1 stream with the Orphan stream and other Galactic observations, cannot constrain the halo shape to better than  $\simeq 25\%$ .

A large portion of this uncertainty arises from our consideration of the halo orientation. A single, short stream is mostly sensitive to the projection of the halo onto the stream. This lack of sensitivity to the total halo gives a great deal of freedom to its axis ratios. As the stream size increases, or as more streams are considered, a greater portion of the Galaxy is explored, giving more sensitivity to the total halo and reducing the uncertainty in the halo parameters. Related to this point, recent studies suggest that streams containing turning points are particularly sensitive the halo shape (Varghese et al. 2011; Lux et al. 2012). In this work we only considered mock GD-1 and Orphan streams which do not contain such turning points. Other, shorter, streams like Pal 5 and NGC 5466 may be more promising than our results suggest if turning points in the streams are found.

These results suggest that the path to improved inferences of the halo structure is to fit all available streams and other Galactic observations simultaneously. There remains, however, the issue that the map from gravitational potential to stream is not as simply as the orbit-fitting technique deployed in this paper. How one explores the full range of Galactic models while properly accounting for stream dynamics remains an outstanding challenge.

Nonetheless, the central points of this work remains true regardless of the stream modelling technique. Stellar

streams provide powerful probes of the Galactic structure, but they must be combined with a suite of other observational constraints to reach their full potential. It is necessary to fully explore the model parameter space as model degeneracies may cause errors in the inferred quantities depending on the assumed quantities. Finally, the degeneracies in the model parameters can be reduced through the use of extended streams or multiple streams, yielding better models of the MW.

L.M.W. is supported by the Natural Sciences and Engineering Research Council of Canada through a Discovery Grant.

## REFERENCES

- Allgood B., Flores R. A., Primack J. R., Kravtsov A. V., Wechsler R. H., Faltenbacher A., Bullock J. S., 2006, *MNRAS*, 367, 1781
- Belokurov V. et al., 2014, *MNRAS*, 437, 116
- Belokurov V. et al., 2007, *ApJ*, 658, 337
- Belokurov V. et al., 2006, *ApJ*, 642, L137
- Belokurov V., Evans N. W., Irwin M. J., Hewett P. C., Wilkinson M. I., 2006, *ApJ*, 637, L29
- Binney J., Gerhard O., Spergel D., 1997, *MNRAS*, 288, 365
- Binney J., Tremaine S., 2008, *Galactic Dynamics: Second Edition*. Princeton Univ. Press, Princeton, NJ
- Bovy J., Hogg D. W., Rix H.-W., 2009, *ApJ*, 704, 1704
- Brand J., Blitz L., 1993, *A&A*, 275, 67
- Courteau S. et al., 2013, arXiv:1309.3276 [astro-ph.CO]
- Debattista V. P., Roškar R., Valluri M., Quinn T., Moore B., Wadsley J., 2013, *MNRAS*, 434, 2971
- Deg N., Widrow L., 2013, *MNRAS*, 428, 912
- Demers S., Battinelli P., 2007, *A&A*, 473, 143
- Dehnen W., Binney J., 1998, *MNRAS*, 294, 429
- Einasto J., 1965, *Trudy Inst. Astrofiz. Alma-Ata*, 5, 87
- Feast M., Whitelock P., 1997, *MNRAS*, 291, 683
- Fellhauer M. et al., 2006, *ApJ*, 651, 167
- Foreman-Mackey D., Hogg D. W., Lang D., Goodman J., 2012, arXiv:1202.3665 [astro-ph.IM]
- Franx M., Illingworth G., de Zeeuw T., 1991, *ApJ*, 383, 112
- Frenk C. S., 1994, in Audouze J., Pelletan M.-C., & Szalay S., eds *Proc. IAU Symp.*, 130, Large Scale Structures of the Universe, p. 259
- Flynn C., Fuchs B., 1994, *MNRAS*, 270, 471
- Goodman J., Weare J., 2010, *Comm. App. Math. Comp. Sci.*, 65, 5
- Gregory P. C., 2005, *Bayesian Logical Data Analysis for the Physical Sciences: A Comparative Approach with ‘Mathematica’*. Cambridge Univ. Press, Cambridge, UK
- Grillmair C. J., 2006, *ApJ*, 645, L37
- Grillmair C. J., Dionatos O., 2006, *ApJ*, 641, L37
- Grillmair C. J., Dionatos O., 2006, *ApJ*, 643, L17
- Grillmair C. J., Johnson R., 2006, *ApJ*, 639, L17
- Helmi A., 2004, *ApJ*, 610, L97
- Holmberg J., Flynn C., 2004, *MNRAS*, 352, 440
- Ibata R. A., Wyse R. F. G., Gilmore G., Irwin M. J., Suntzeff N. B., 1997, *AJ*, 113, 634
- Ibata R., Lewis G. F., Irwin M., Totten E., Quinn T., 2001, *ApJ*, 551, 294
- Ibata R., Lewis G. F., Martin N. F., Bellazzini M., Correnti M., 2013, *ApJ*, 765, L15
- Jing Y. P., Suto Y., 2002, *ApJ*, 574, 538
- Johnston K. V., Law D. R., Majewski S. R., 2005, *ApJ*, 619, 800
- Kochanek C. S., 1996, *ApJ*, 457, 228
- Koposov S. E., et al., 2012, *ApJ*, 750, 80
- Koposov S. E., Rix H.-W., Hogg D. W., 2010, *ApJ*, 712, 260
- Kuijken K., Dubinski J., 1995, *MNRAS*, 277, 1341
- Kuijken K., Gilmore G., 1991, *ApJ*, 367, L9
- Küpper A. H. W., Lane R. R., Heggie D. C., 2012, *MNRAS*, 420, 2700
- Law D. R., Johnston K. V., Majewski S. R., 2005, *ApJ*, 619, 807
- Law D. R., Majewski S. R., Johnston K. V., 2009, *ApJ*, 703, L67
- Law D. R., Majewski S. R., 2010, *ApJ*, 714, 229
- Lin D. N. C., Jones B. F., Klemola A. R., 1995, *ApJ*, 439, 652
- Lux H., Read J. I., Lake G., Johnston K. V., 2013, *MNRAS*, 436, 2386
- Lux H., Read J. I., Lake G., Johnston K. V., 2012, *MNRAS*, 424, L16
- Lux H., Read J. I., Lake G., 2010, *MNRAS*, 406, 2312
- Malhotra, S., 1995, *ApJ*, 448, 138
- Majewski S. R., Skrutskie M. F., Weinberg M. D., Osthheimer J. C., 2003, *ApJ*, 599, 1082
- Martínez-Delgado D., Gómez-Flechoso M. Á., Aparicio, A., Carrera R., 2004, *ApJ*, 601, 242
- Merritt D., Navarro J. F., Ludlow A., Jenkins A., 2005, *ApJ*, 624, L85
- Newberg H. J., Willett B. A., Yanny B., Xu Y., 2010, *ApJ*, 711, 32
- Odenkirchen M. et al., 2001, *ApJ*, 548, L165
- Peñarrubia J., Belokurov V., Evans N. W., Martínez-Delgado D., Gilmore G., Irwin M., Niederste-Ostholt M., Zucker D. B., 2010, *MNRAS*, 408, L26
- Perryman, M. A. C. et al., 2001, *A&A*, 369, 339
- Prugniel P., Simien F., 1997, *A&A*, 321, 111
- Reid M. J. et al., 2009, *ApJ*, 700, 137
- Terzić B., Graham A. W., 2005, *MNRAS*, 362, 197
- Tremaine S. et al. 2002, *ApJ*, 574, 740
- Sanders J. L., Binney J., 2013, *MNRAS*, 433, 1813
- Sanders J. L., Binney J., 2013, *MNRAS*, 433, 1826
- Vera-Ciro C., Helmi A., 2013, *ApJ*, 773, L4
- Varghese A., Ibata R., Lewis G. F. 2011, *MNRAS*, 417, 198
- Warren M. S., Quinn P. J., Salmon J. K., Zurek W. H., 1992, *ApJ*, 399, 405
- Widrow L. M., Pym B., Dubinski J., 2008, *ApJ*, 679, 1239
- Willett B. A., Newberg H. J., Zhang H., Yanny B., Beers T. C., 2008, *ApJ*, 679, 1239
- Zhao H., 2004, *MNRAS*, 351, 891

## 9 APPENDIX: EMCEE ON A SPHERE

Our Galactic model has three Euler angles and triaxial symmetry. The first two Euler angles specify the angular position of the intermediate axis. Therefore, when the EMCEE algorithm stretches between two walkers it should be along the great circle connecting the two intermediate axes. Additionally, the triaxial symmetry introduces a number of degeneracies in the Euler angles. Since the pole and anti-pole of



an axis provide identical models, the stretch should be along the shortest arc connecting the pole or anti-pole of the second walker's intermediate axis to the first walker axis.

To achieve this, we modify the EMCEE algorithm in a straightforward manner. For a given pair of walkers, the location of the intermediate axes on a sphere are found. These two points are then rotated to a coordinate system,  $(\lambda', \beta')$ , that has one of the points at  $\beta' = 90^\circ$ . In this coordinate system, the great circle connecting the two points has a constant  $\lambda'$  so the stretch is only in  $\beta'$ . If the second walker has  $\beta' > 0$  then the stretch is between those two points. Otherwise, we replace the second point with its anti-pole for the stretch. The proposal is then generated along the arc connecting the appropriate pair of points and rotated back to the original coordinate system to give the proposal Euler angles. This technique removes the degeneracies in the first two Euler angles and stretches along the great circle between two points on a sphere.

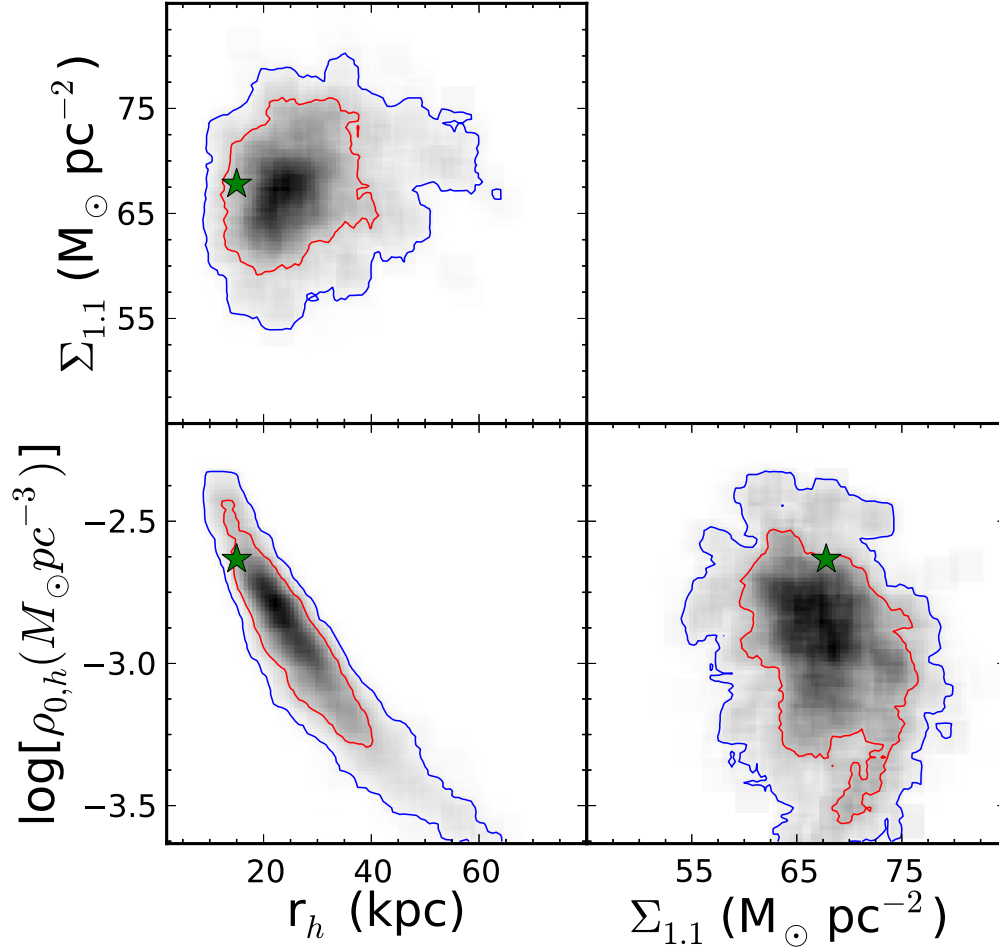


**Figure 1.** PDFs of the halo scale density, halo scale length, and local vertical force,  $\Sigma_{1.1}$  where  $\Sigma_{1.1} = |K_z(1.1\text{kpc})|/2\pi G$ . The lower left panel shows the relation between the halo scale density and scale length, the upper left panel shows the local vertical force and the scale length, and the lower right panel shows the local vertical force and scale density. The red and blue contour lines are the one and two sigma limits of the PDFs. The green star indicates the value of the generative parameter and the data constraint.

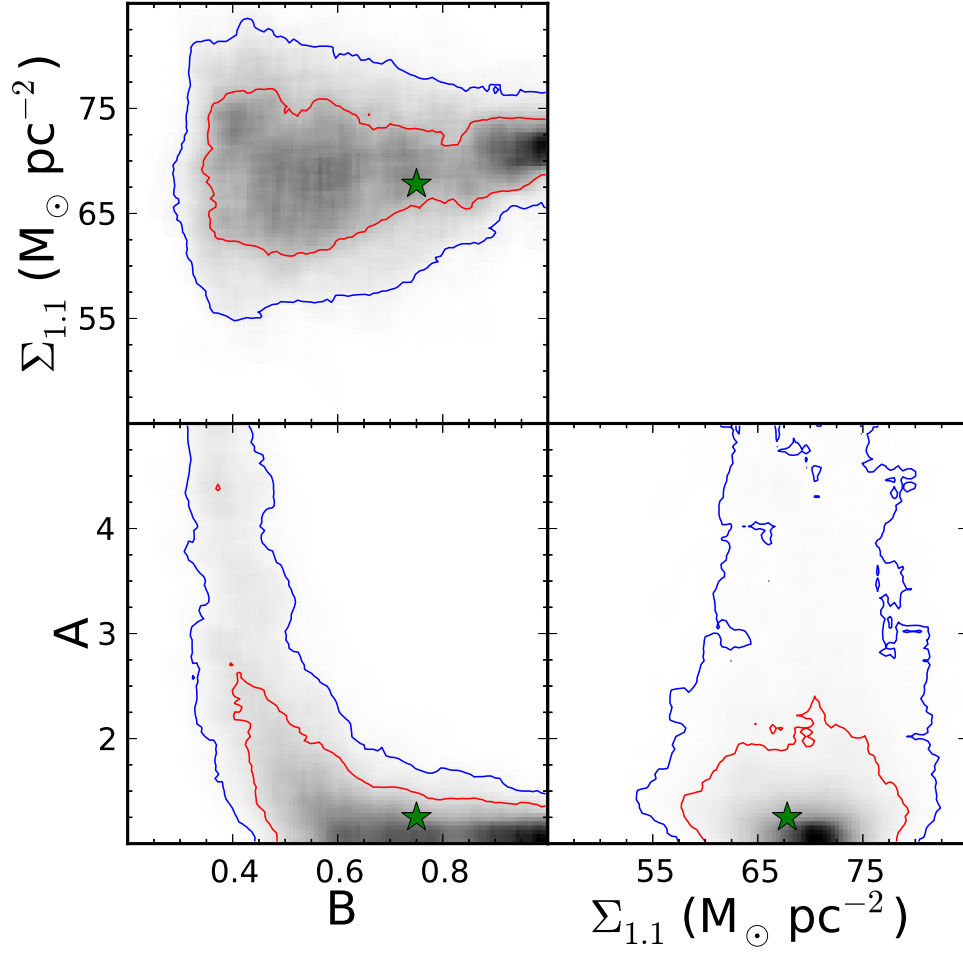


**Figure 2.** PDFs of the halo axis ratios and local vertical force. The lower left panel shows the relation between the  $A$  and  $B$ , the upper left panel shows the local vertical force and  $B$ , and the lower right panel shows the local vertical force and  $A$ . The contours, green stars, and  $\Sigma_{1.1}$  are as in Figure 1.

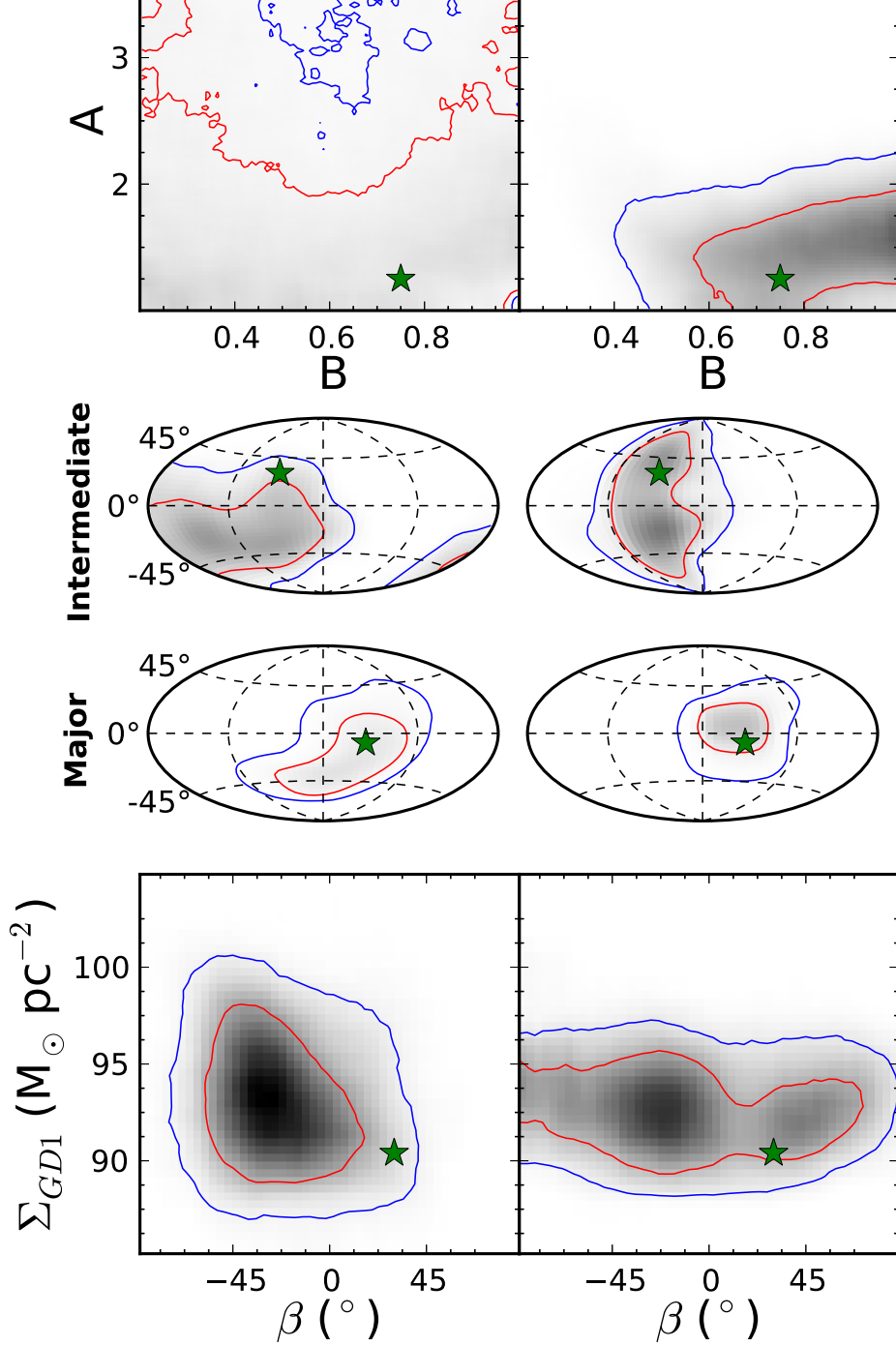


**Figure 3.** The inferred shape, orientation and force at the GD-1 progenitor particle's location PDFs. In this figure  $\Sigma_{GD1} = |F|(\text{GD-1})/2\pi G$ . The first column uses only the stream information. The second column uses both the stream and non-stream data simultaneously. The first row shows the inferred shape.  $A$  is the major/intermediate axis ratio and  $B$  is the minor/intermediate ratio. The second row shows the location of the intermediate axis in angular coordinates centered on the Galactic Center with the Sun at along the  $(0^\circ, 0^\circ)$  line. The third row shows the location of the major axis in that same coordinate system. The minor axis lies perpendicular to the major and intermediate axes. The bottom row shows the total force at the GD-1 progenitor compared to the latitude of the inferred intermediate axis. The units of the force are  $M_\odot \text{ pc}^{-2}$ . The green and contours are as in Figure 1. Each row uses the same color map limits to highlight the differences between the use of the different sets of constraints. Additionally the bottom three rows have had the pole and anti-pole points stacked together as they are equivalent. The dashed black lines in the Aitoff plots are at longitudes of  $(-90^\circ, 0^\circ, 90^\circ)$  and latitudes of  $(-45^\circ, 0^\circ, 45^\circ)$ .

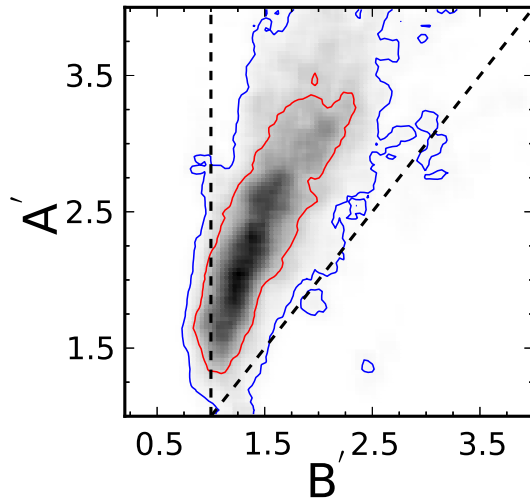


**Figure 4.** The inferred shape using the  $70^\circ$  GD-1 stream and the standard suite of constraints. In this analysis all parameters are allowed to vary with the exception that one axis lies perpendicular to the disk and the other two are in the plane of the disk.  $A'$  is ratio of the larger to the smaller disk axes.  $B'$  is the ratio of the perpendicular axis to the smaller disk axis. The contours are the same as in Figure 1. The dashed lines separate the parameter space into regions where the perpendicular axis is the minor axis ( $B' < 1$ ) and where the perpendicular axis is the major axis ( $B' > A'$ ).

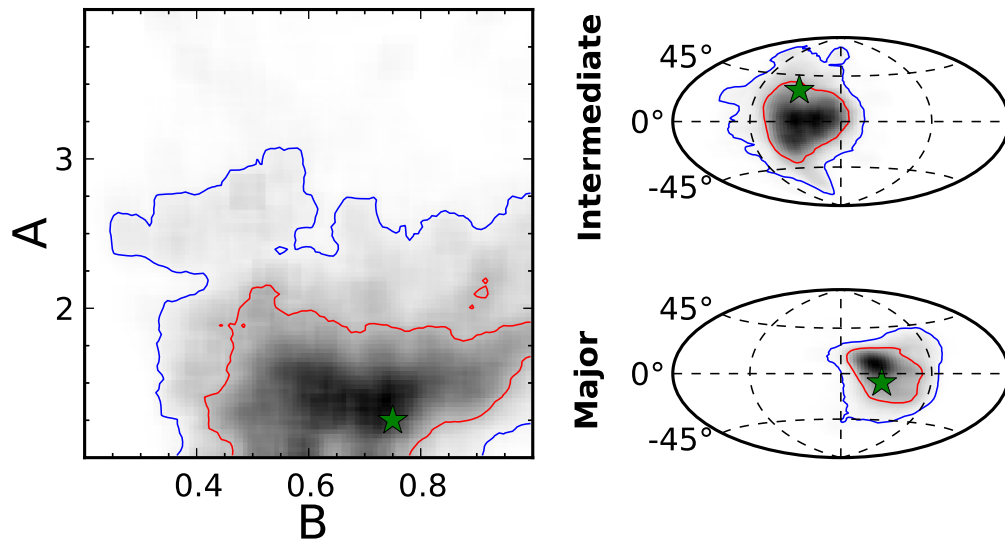


**Figure 5.** The inferred shape and orientation PDFs using the 70° GD-1 stream and the standard suite of constraints and allowing all parameters to vary. The contours and green stars are as in Figure 1 and the Aitoff axes are as in Figure 3.

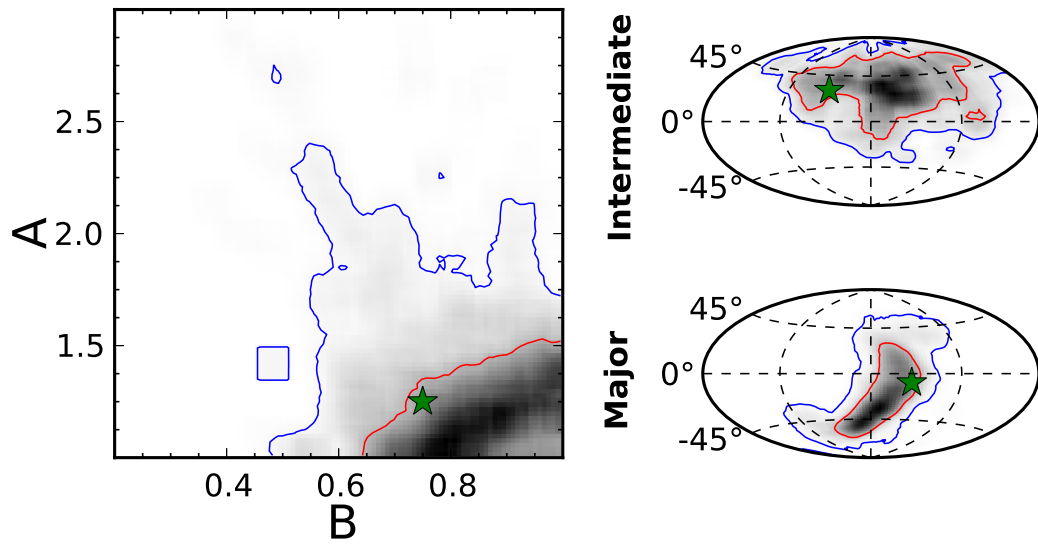


**Figure 6.** The inferred shape and orientation PDFs using the  $180^\circ$  GD-1 stream and the standard suite of constraints and allowing all parameters to vary. The contours and green stars are as in Figure 1 and the Aitoff axes are as in Figure 3.

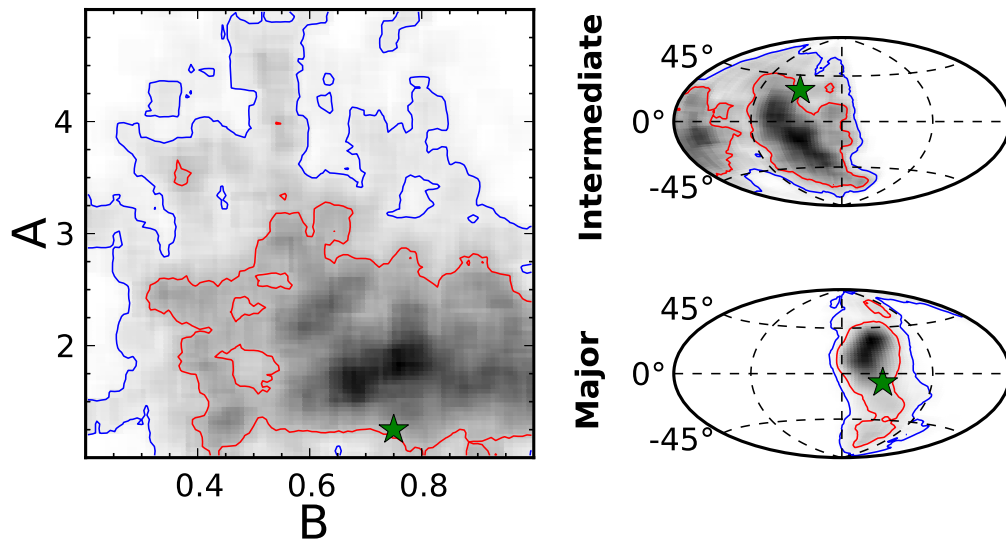


**Figure 7.** The inferred shape and orientation PDFs using the  $60^\circ$  Orphan-like stream and the standard suite of constraints and allowing all parameters to vary. The contours and green stars are as in Figure 1 and the Aitoff axes are as in Figure 3.



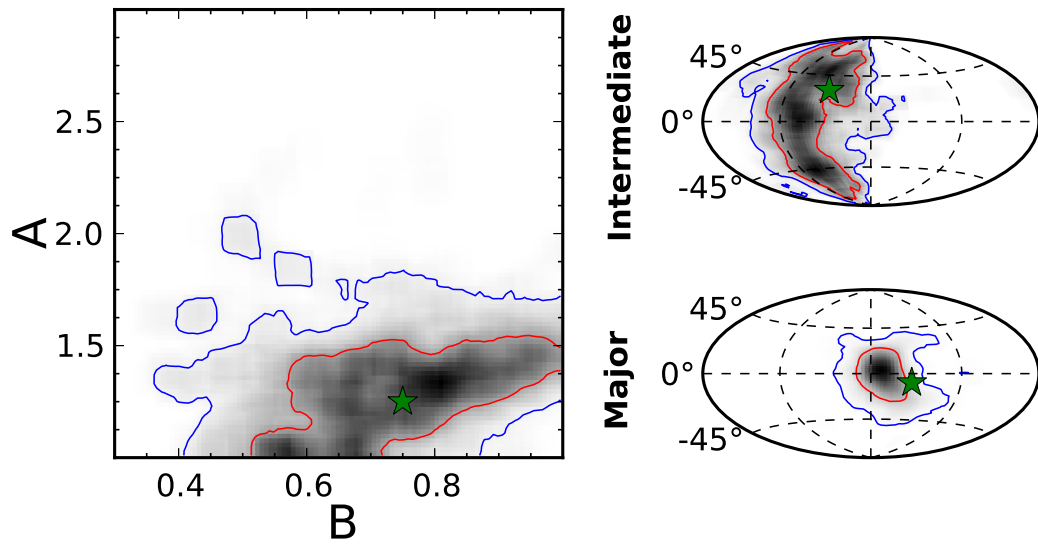


**Figure 8.** The inferred shape and orientation PDFs using the 70° GD-1 and the 60° Orphan streams and the standard suite of constraints and allowing all parameters to vary. The contours and green stars are as in Figure 1 and the Aitoff axes are as in Figure 3.